

Global Stokes Drift Climate under the RCP8.5 Scenario

ØYVIND BREIVIK,^{a,b,g} ANA CARRASCO,^c JOANNA STANEVA,^d ARNO BEHRENS,^d
ALVARO SEMEDO,^e JEAN-RAYMOND BIDLOT,^f AND OLE JOHAN AARNES^c

^a Norwegian Meteorological Institute, Bergen, Norway

^b University of Bergen, Bergen, Norway

^c Norwegian Meteorological Institute, Oslo, Norway

^d Helmholtz Zentrum Geesthacht, Geesthacht, Germany

^e IHE Delft, Delft, Netherlands

^f European Centre for Medium-Range Weather Forecasts, Reading, United Kingdom

(Manuscript received 7 July 2018, in final form 1 December 2018)

ABSTRACT


The future Stokes drift climate is investigated using a global wave climate projection (2071–2100) forced with EC-EARTH winds under the RCP8.5 scenario. The future climate run is compared against a historical run (1976–2005). The Stokes drift climate is analyzed in terms of Stokes transport and surface Stokes drift. The impact on Stokes drift from changes to the wind, wind sea, and swell climate is identified. The consequences for upper-ocean mixing and circulation are studied by investigating the turbulent Langmuir number and the Stokes depth. The historical climate run is also compared to a hindcast with ERA-Interim forcing. Systematic discrepancies due to differences in resolution and model physics are identified, but no fundamental weaknesses are uncovered that should adversely affect the future run. As the surface Stokes drift is largely dictated by high-frequency waves, it is to a great degree controlled by changes to the local wind field, whereas the Stokes transport is more sensitive to swell. Both are expected to increase in the Southern Ocean by about 15%, while the North Atlantic sees a decrease of about 10%. The Stokes depth and the turbulent Langmuir number are set to change by about $\pm 20\%$ and $\pm 10\%$, respectively. The changes to the Stokes depth suggest a deeper impact of the Coriolis–Stokes force in the Southern Ocean and a decrease in the northern extratropics. Changes to the KPP Langmuir-enhancement factor suggests potentially increased mixing in the Southern Ocean and a reduction in the North Atlantic and the North Pacific.

1. Introduction

Wind-generated ocean surface gravity waves, referred to simply as waves, are important to climate projections because they modulate the exchange of momentum, heat, and mass between oceans and atmosphere (e.g., Cavalieri et al. 2012; Hemer et al. 2013) and because of their influence on all aspects of coastal (Cavalieri et al. 2018) and offshore activities, such as coastal erosion, flooding, and sediment budgets, and the loads imposed on offshore

structures and moving vessels (Bitner-Gregersen et al. 2018).

The wave-induced Stokes drift (Stokes 1847; van den Bremer and Breivik 2017) is essential for calculating the trajectories of oil spills (Jones et al. 2016) and drifting objects (Röhrs et al. 2012; Breivik et al. 2013; Röhrs et al. 2015). The Stokes drift contributes to the advection of momentum and tracers on the near-surface ocean (Ardhuin et al. 2009; Röhrs et al. 2014; Dagestad et al. 2018; Strand et al. 2018) and influences the upper-ocean circulation through generation of Langmuir turbulence (e.g., Belcher et al. 2012; D’Asaro et al. 2014; Fan and Griffies 2014; Li et al. 2016, 2017) as well as the Coriolis–Stokes forcing (e.g., Breivik et al. 2015; Suzuki and Fox-Kemper 2016; Alari et al. 2016; Staneva et al. 2017). How changes to the wave climate will alter the Stokes drift and the associated depth-integrated Stokes transport in the future is thus of practical and scientific interest.

 Denotes content that is immediately available upon publication as open access.

^g ORCID: 0000-0002-2900-8458.

Corresponding author: Øyvind Breivik, oyvind.breivik@met.no

DOI: 10.1175/JCLI-D-18-0435.1

© 2019 American Meteorological Society. For information regarding reuse of this content and general copyright information, consult the AMS Copyright Policy (www.ametsoc.org/PUBSReuseLicenses).

The Stokes drift profile can be calculated from the two-dimensional spectrum (Kenyon 1969), but this is rarely done in ocean modeling because of the exorbitant cost of integrating the wave model spectrum at every vertical level required by the ocean model. Instead, approximate Stokes drift profiles are usually employed that depend on the surface Stokes drift and the Stokes transport (Breivik et al. 2014, 2016; Li et al. 2017).

Recently, several studies have appeared that employ near-surface winds from phase 5 of the Coupled Model Intercomparison Project (CMIP5) to investigate changes to the future wave climate. Aarnes et al. (2017), using wind fields from ensemble members of six different CMIP5 models to force a wave model, found that the majority of the models studied exhibited a decrease in wind speed and associated wave height in the North Atlantic region. Shimura et al. (2016) saw a similar trend in the western North Pacific. Wang et al. (2014), using a statistical method to relate the wind and pressure fields of 20 CMIP5 models to the local significant wave height, found that the Southern Ocean will experience an increase in wind speed and wave height, while the North Pacific and the North Atlantic will mainly see a decrease in both wind speed and wave height, broadly consistent with the findings of Aarnes et al. (2017) and Shimura et al. (2016). These studies focused on changes in the significant wave height climate toward the end of the twenty-first century. The aim of the present study is to investigate the impact of the projected changes, under the RCP8.5 scenario, on the surface Stokes drift and the depth-integrated Stokes transport as well as the consequences for two quantities commonly used to model wave impact on the mixed layer, namely, the turbulent Langmuir number and the Stokes depth. The RCP8.5 scenario has the highest greenhouse gas emissions forcing of the four scenarios commonly studied under CMIP5, with a constant positive emission trend from 2005 to 2100. Under this scenario the global mean surface temperature for 2081–2100 relative to 1986–2005 is projected to be in the range from 2.6° to 4.8°C and the Arctic is expected to warm even faster (Stocker et al. 2013). We chose a high-emission scenario in order to investigate the maximum change that can be expected for the wave climate as well as its impact on upper-ocean mixing and circulation.

The paper is organized as follows. The wave quantities to be studied are presented in section 2. In section 3, we describe the wave model setup and briefly compare the historical wave climate integration against an ERA-Interim-forced wave hindcast (discussed further in the appendixes). Section 4 reports the major differences between the historical and future climate run. In section 5, we discuss the consequences for the Stokes depth and

the turbulent Langmuir number. Finally, some conclusions are drawn about the consequences of the future Stokes drift climate in section 6.

2. Stokes drift, Stokes transport, Stokes depth, and the turbulent Langmuir number

The deep-water Stokes drift (assuming the deep-water dispersion relation $\omega^2 = gk$), following the notation by Breivik et al. (2014), is written as

$$\mathbf{v}_s(z) = \frac{16\pi^3}{g} \int_0^{2\pi} \int_0^\infty f^3 \hat{\mathbf{k}} e^{2kz} F(f, \theta) df d\theta. \quad (1)$$

Here θ is the wave direction measured clockwise from north and $f = \omega/2\pi$. In the deep-water limit, the Stokes transport $\mathbf{V}_s = \int_{-\infty}^0 \mathbf{v}_s(z) dz$ becomes

$$\mathbf{V}_s = 2\pi \int_0^{2\pi} \int_0^\infty f \hat{\mathbf{k}} F(f, \theta) df d\theta. \quad (2)$$

The integral here is the first-order moment of the wave spectrum m_1 weighted by the unit vector $\hat{\mathbf{k}}$ of the wave component. As the wave model does not calculate the Stokes transport, we estimate it from m_1 [see Eq. (35) in Breivik et al. (2014)],

$$V_s \approx 2\pi m_1 = \frac{2\pi H_s^2}{16T_{m_{01}}}. \quad (3)$$

Here $T_{m_{01}} = m_0/m_1$ is the first-moment mean wave period (Holthuijsen 2007) and $H_s = 4\sqrt{m_0}$. The Stokes transport is always less than $2\pi m_1$, see Eq. (34) in Breivik et al. (2014), but even in multidirectional seas the Stokes transport is only slightly smaller than $2\pi m_1$ (about 16%). This leads to a modest, but consistent, overestimation of the Stokes transport in both the historical and the future climate integrations as well as the hindcast run.

The surface Stokes drift [$z = 0$ in Eq. (1)] is proportional to the third moment m_3 and heavily weighted by the higher frequencies. It is therefore more dominated by locally generated wind sea than by low-frequency swell. Changes to the surface Stokes drift are for this reason expected to be more in tune with changes to the wind field. With depth, the wave field is “filtered” as a given wave frequency has an e -folding depth of $(2k)^{-1}$ in Eq. (1), and swell will consequently dominate the deeper levels. The Stokes transport is more sensitive to changes in swell patterns than the surface Stokes drift as it is proportional to m_1 ; see, for example, Carrasco et al. (2014).

The Stokes production term in the turbulence kinetic energy (TKE) equation (Li and Garrett 1997; Flór et al. 2010) is related to the Stokes drift shear. The TKE equation, following the notation of Breivik et al. (2016), is written

$$\frac{De}{Dt} = \underbrace{K_m S^2}_{\text{Shear production}} - K_h N^2 + \underbrace{K_m \mathbf{S} \cdot \frac{\partial \mathbf{v}_s}{\partial z}}_{\text{Stokes production}} - \frac{\partial}{\partial z} (\overline{w'e}) - \frac{1}{\rho_w} \frac{\partial}{\partial z} (\overline{w'p'}) - \varepsilon. \quad (4)$$

Here e is the turbulent kinetic energy per unit mass; $\overline{w'e}$ and $\overline{w'p'}$ are the turbulent transport and pressure correlation terms (Stull 1988; Kantha and Clayson 2000). The Eulerian shear (marked) and the buoyancy production terms are $\mathbf{S} \cdot \mathbf{S} = S^2 = (\partial \bar{\mathbf{u}}/\partial z)^2$ and $N^2 = -(g/\rho_w) d\rho_w/dz$, respectively, where $K_{h,m}$ are turbulent diffusion coefficients. Finally, ε represents dissipation of turbulent kinetic energy. It is the third term, Stokes production, that represents Langmuir turbulence.

How the Stokes drift profile varies with Stokes transport and surface Stokes drift can best be investigated by looking at the Stokes depth δ_s . For a monochromatic (exponential) Stokes drift profile, this represents its e -folding depth and is related to the wavenumber as $\delta_s = 1/(2\bar{k})$, see Polton et al. (2005) and Kukulka and Harcourt (2017). This can be written as the ratio of the Stokes transport to the surface Stokes drift,

$$\delta_s = V_s / v_{s_0}, \quad (5)$$

and is calculated straight from the wave model parameters. The Stokes depth is the scale depth to which the Stokes drift penetrates (Polton et al. 2005), determining the thickness of the layer that is influenced by the Coriolis–Stokes force,

$$\frac{D\mathbf{u}}{Dt} = -\frac{1}{\rho_w} \nabla p + (\mathbf{u} + \mathbf{v}_s) \times f \hat{\mathbf{z}} + \frac{1}{\rho_w} \frac{\partial \boldsymbol{\tau}}{\partial z}. \quad (6)$$

Here \mathbf{u} is the horizontal Eulerian current vector, f the Coriolis frequency, $\hat{\mathbf{z}}$ the upward unit vector, p the pressure, and $\boldsymbol{\tau}$ the stress.

The turbulent Langmuir number, first introduced by McWilliams et al. (1997), is defined as $\text{La}_t = \sqrt{u_* v_{s_0}}$, where u_* is the water-side friction velocity. Its square approximates the ratio of the Eulerian shear and Stokes production terms in Eq. (4) [see also Eq. (2) in Belcher et al. 2012]. It is commonly used (Fan and Griffies 2014; Li et al. 2016) to include a Langmuir-enhancement factor F_{LT} in the turbulent velocity scale W of the K-profile turbulence parameterization (KPP; Large et al. 1994),

$$W = \frac{\kappa u_*}{\Phi} F_{\text{LT}}. \quad (7)$$

Here κ is von Kármán's constant, and Φ is the Monin–Obukhov stability function. The first and most widely

tested (Fan and Griffies 2014; Li et al. 2016; Malila 2017; Ali et al. 2018, manuscript submitted to *Ocean Modell.*) parameterization was proposed by McWilliams and Sullivan (2000),

$$F_{\text{LT}} = \left(1 + \frac{C_w}{\text{La}_t^{2\alpha}} \right)^{1/\alpha}. \quad (8)$$

The empirical constants C_w and α are assumed positive [0.08 and 2, respectively, were proposed by McWilliams and Sullivan (2000)]. The K in KPP is assumed to be a function of the depth of the mixed layer h_{bl} and the turbulent velocity scale whose profile is dictated by a function G across the mixed layer,

$$K = h_{\text{bl}} W G. \quad (9)$$

When the turbulent Langmuir number is small (i.e., when Stokes drift shear dominates over Eulerian shear; Belcher et al. 2012; Sutherland et al. 2014), W becomes large, boosting the turbulent diffusion coefficient. Several Langmuir-enhancement factors have since been explored (all approximately proportional to an inverse power of La_t), notably by Smyth et al. (2002), Li et al. (2005), Harcourt and D'Asaro (2008), Takaya et al. (2010), Van Roekel et al. (2012), and Li and Fox-Kemper (2017). The global study by Fan and Griffies (2014) of the parameterizations by McWilliams and Sullivan (2000) and Smyth et al. (2002) as well as the study by Li et al. (2016) and recent studies of all of the aforementioned parameterizations by Malila (2017) and Ali et al. (2018, manuscript submitted to *Ocean Modell.*) show that the mixed layer is quite sensitive to the specific choice of empirical formula, and that Eq. (8) yields too strong mixing, especially during winter deep convection events. This means that relatively small changes to the turbulent Langmuir number could make a difference to the mixed layer properties of the ocean model. However, changes to La_t may also have a small effect if the turbulent Langmuir number is already well above the level where Langmuir turbulence is thought to dominate (around 0.3; Belcher et al. 2012), as the mixing due to Langmuir turbulence is negligible in this end of the regime diagram (see Fig. 3 by Belcher et al. 2012). The intensity of Langmuir mixing is more sensitive to the changes to La_t for smaller values (i.e., $\text{La}_t < 0.3$) than for larger values ($\text{La}_t \sim 1$) and parameterizations of Langmuir-enhanced mixing that are based on these scaling laws are sensitive to changes of La_t for smaller values than 0.3 and therefore also sensitive to the exact formula of the enhancement factor (e.g., Li et al. 2016).

The choice of Langmuir-enhancement factor will clearly affect the impact that changes to the Stokes drift

TABLE 1. Features of the climate and the hindcast runs.

	Climate runs	Hindcast
WAM	WAM CY4.5.3	EC-WAM cycle 43R3 (CY43R3) with Ardhuin et al. (2010) physics (ST4)
Type of run	Past climate and RCP8.5	EC-WAM stand-alone global hindcast
Winds and ice from	EC-EARTH	10 m, neutral
Spectral resolution	25 frequencies: 0.0418–0.4115 Hz 24 directions (15°)	30 frequencies: 0.0345–0.5476 Hz 24 directions (15°)
SD integration	Trapezoidal rule	Simpson integration scheme
Output time step	6 h	1 h
Spatial resolution	1°	0.36°
Period	1976–2005 and 2071–2100	1999–2017

climate will have on ocean models. Although known to overestimate the mixing ([Fan and Griffies 2014](#); [Li et al. 2016](#)), we choose to investigate the parameterization [Eq. (9)] in [McWilliams and Sullivan \(2000\)](#) as it is the one most commonly tested. We refrain from investigating more parameterizations here as the full impact on upper-ocean mixing can only be studied using fully coupled atmosphere–wave–ocean climate models.

There exist a few studies of the impact of Langmuir turbulence in ocean models that employ a TKE mixing scheme (as opposed to KPP; e.g., [Janssen 2012](#); [Noh et al. 2016](#)), but as there is currently no straightforward way to employ La_t in a one-equation TKE scheme, it is unclear how models of this vein could be compared against models that employ KPP, and we do not consider one- or two-equation TKE schemes here.

3. Wave model configuration

A global wave model (WAM; [Hasselmann et al. 1988](#); [Komen et al. 1994](#)) was forced with 10-m winds from the global climate CMIP5 EC-EARTH model. The EC-EARTH general circulation model is a fully coupled atmosphere–ocean–sea ice system climate model developed from the ECMWF operational seasonal forecast system 3 ([Hazeleger et al. 2010, 2012](#)). Ice cover was also taken from EC-EARTH. Two climate integration periods, each 30 years, were studied. The first is the period 1976–2005, referred to as the “historical” run. This integration uses the observed greenhouse gas concentrations over the period. The second is denoted the “future” run. Here we have chosen the period at the end of the twenty-first century (2071–2100) under the RCP8.5 scenario (see [Table 1](#) for an overview of the model setups). WAM is a third-generation wave model, and the version used here is the cycle 4.5.3 (CY4.5.3), an update of the WAM, cycle 4, described by [Komen et al. \(1994\)](#). Cycle 4.5.3 includes a source function integration scheme developed by [Hersbach and Janssen \(1999\)](#), with a new semi-implicit approach developed at the ECMWF. The model updates of

EC-WAM described by [Bidlot et al. \(2007\)](#) are also included.

The model was run with a directional resolution of 15° and 25 frequencies, ranging from 0.042 to 0.41 Hz with logarithmic 10% increments (corresponding to wavelengths between 10 and 885 m). The model domain is global with a resolution of 1° × 1° and output every 6 h. The following analysis on wind speed and wave model parameters was done on daily means. The surface Stokes drift speed was calculated from vector quantities, but all analysis was done on scalar averages. Unidirectional Stokes transport V_s magnitude was calculated using Eq. (3), since vectorial Stokes transport is not an output parameter in the wave models.

We have compared the historical run to an EC-WAM ([ECMWF 2016](#)) hindcast forced with ERA-Interim (1999–2017) winds ([Dee et al. 2011](#)). This wave model integration (referred to as the “hindcast”) is run at higher resolution (approximately 0.36° × 0.36°) and covers a larger spectral range (see [Table 1](#)). The hindcast was chosen because the Stokes drift is not directly available from the ERA-Interim archive, but also because it was run with a new, experimental version of EC-WAM with wave physics based on the source term package 4 (ST4) parameterization introduced by [Ardhuin et al. \(2010\)](#), which shows superior swell damping in the tropics. The wave models thus differ in their model physics, notably the swell-damping scheme in EC-WAM, and in their different wind input source terms. A detailed account of the differences between the historical climate model integration and the hindcast are given in [appendix A](#).

Although there are notable differences between the two wave model integrations, the general features of the past climate of the surface Stokes drift, significant wave height, and the Stokes transport are well represented by the historical run. The differences are understood and are mostly associated with discrepancies in the wind field, the swell attenuation schemes, and subgrid topographic features. Importantly, differing spectral ranges and resolution affect the average surface Stokes drift (see [appendix A](#)). However, these resolution-dependent

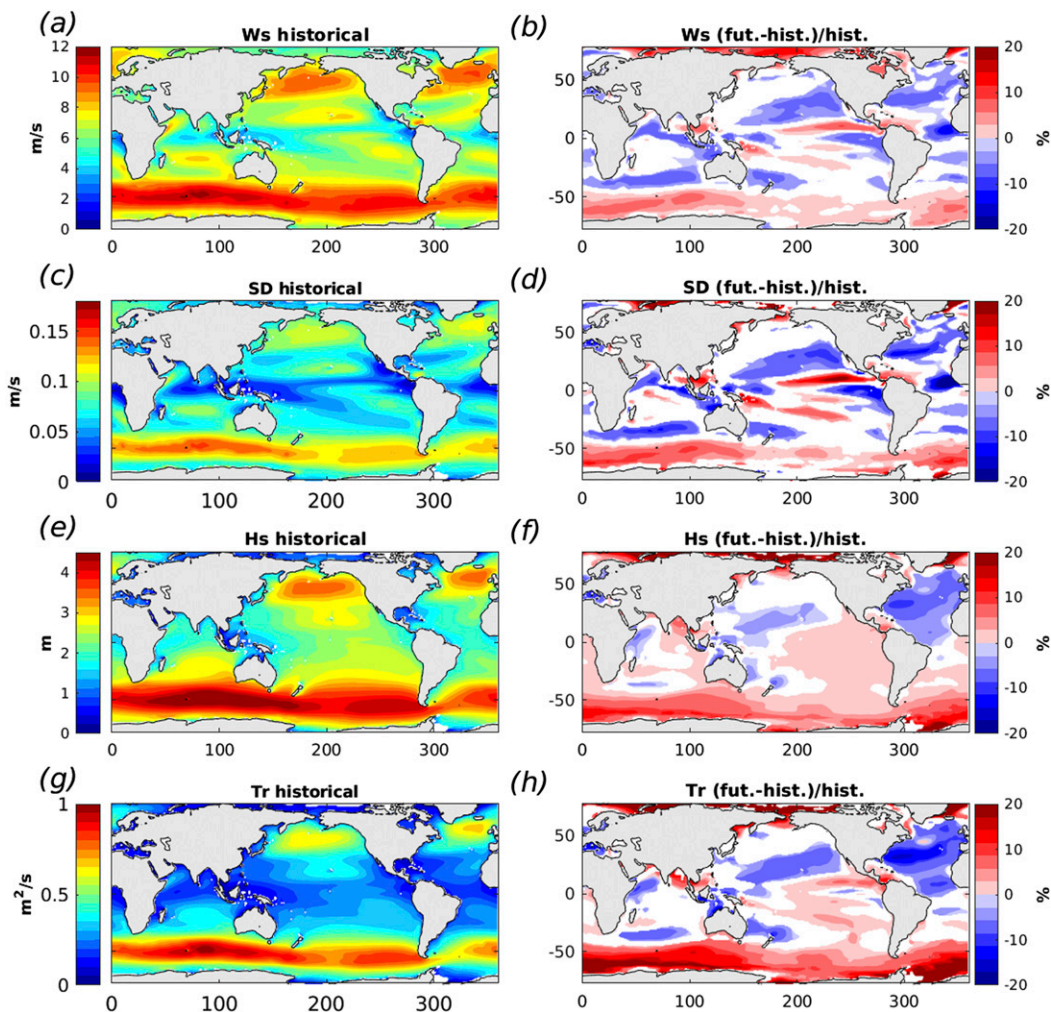


FIG. 1. (a) Average 10-m wind speed U_{10} , (c) Stokes drift speed v_{s0} , (e) significant wave height H_s , and (g) Stokes transport V_s from the historical run (1976–2005) and (b),(d),(f),(h) the normalized difference (%) between the future RCP8.5 run (2071–2100) and the historical run. Only the regions statistically different with a significance level of 0.01 are colored.

differences are qualitatively the same in a future climate. [Appendix B](#) presents the differences at the 95th percentile level and the full probability density functions (PDFs) of U_{10} , H_s , and v_s broken down on geographical regions.

4. EC-EARTH climate projection

[Figure 1](#) summarizes the differences (30-yr averages) between the historical and future integration for wind speed, surface Stokes drift, significant wave height, and Stokes transport. A Wilcoxon rank sum test for paired samples ([Gibbons and Chakraborti 2011](#)) was performed to compare the means of the future run and the historical run. Only regions with statistically significant

differences at the 0.01 level were colored in [Figs. 1b, 1d, 1f, and 1h](#).

The most striking feature in [Figs. 1b, 1d, 1f, and 1h](#) is the projected increase in mean values in the Southern Ocean of all the variables. A slight displacement of the maxima toward the south can also be observed since considerable changes occur south of 60°S , while the maxima in [Figs. 1a, 1c, 1e, and 1g](#) occur along 50°S . Another distinct feature is the projected decrease of mean values in the North Atlantic, which is in agreement with findings by [Aarnes et al. \(2017\)](#).

The projected wind speed ([Figs. 1a,b](#)) shows an increase in the Southern Ocean and a decrease in the northern extratropics. The annual-mean H_s and its projected change ([Figs. 1e,f](#)) exhibit some similarities

with the changes to the wind field in the extratropics. A general decrease is found in the North Atlantic and an increase is observed in the Southern Ocean. Because of the quadratic relation between the H_s of fully developed wind sea and the wind speed (Pierson and Moskowitz 1964), the differences are typically larger for H_s than for U_{10} . The decrease in wind speed in the northern extratropics and the corresponding decrease in significant wave height has been documented for the North Atlantic by Aarnes et al. (2017) and the North Pacific by Shimura et al. (2016). The situation is quite another in the tropics where H_s patterns differ significantly from the wind speed patterns because of remote swell intrusion. The eastern equatorial Pacific (EEP) stands out with a modest wave height increase in the future RCP8.5 scenario.

The impact of changes to the wind field on the surface Stokes drift is evident from Figs. 1c and 1d, and we see changes very similar to those found for the wind speed (Fig. 1b). It is worth noting that the relative change of v_{s0} is greater than that of the wind speed. This is in part because the surface Stokes drift velocity [Eq. (1)] scales as the third spectral moment [see, e.g., Eq. (36) in Breivik et al. (2014)], and will in general increase weakly nonlinearly with the wind speed [see the empirical relation between wind speed and surface Stokes drift; Eq. (7) in Ardhuin et al. (2009)]. It is also related to the fact that wind and waves are in general not in equilibrium (Hanley et al. 2010), and changes in the swell pattern that are uncorrelated with the local wind climate will also affect the surface Stokes drift (although weakly, as it is dominated by the high-frequency part of the spectrum). The Stokes transport (Figs. 1g,h), on the other hand, exhibits a pattern more similar to H_s , which is unsurprising since V_s is proportional to the first spectral moment, and is thus less influenced by the high-frequency part of the spectrum than v_{s0} . The Southern Ocean experiences an increase in both surface Stokes drift and Stokes transport, whereas the North Atlantic and the eastern North Pacific are set to experience a decrease of 15%–20%. The equatorial regions exhibit a more varied pattern, with the surface Stokes drift again mostly responding to changes in the local wind, while the Stokes transport picks up the changing swell patterns. This is evident in the EEP where the significant wave height (Fig. 1f) is increasing because of the increased influx of swell from the Southern Ocean toward the end of the century.

Figure 2 shows the differences between the future RCP8.5 scenario and the historical run at the annual 95th-percentile level calculated from daily means. The differences follow the same general geographical patterns as those of the mean differences (Fig. 1) with an

increase in wind speed in the Southern Ocean and a decrease in the North Atlantic and eastern North Pacific. This is reflected by the changes to the significant wave height, surface Stokes drift, and Stokes transport.

The difference between the future and present swell pattern is presented in Figs. 3a and 3b. Swell is defined in both wave models (EC-WAM and WAM) as spectral wave components whose propagation vector projected on the local wind vector cannot be sustained by the wind speed (ECMWF 2016),

$$1.2 \times 28(u^*/c) \cos(\theta - \phi) \leq 1. \quad (10)$$

Here u^* is the air-side friction velocity and c is the phase speed. The cosine of the angular difference $\theta - \phi$ between the propagation direction of the waves and the local wind direction ensures that wave components traveling at large angles to the local wind are classified as swell. The future swell pattern shows a clear decrease in the North Atlantic and a significant increase in the Southern Ocean. The associated swell Stokes transport shows the same general pattern (Figs. 3c,d). It is clear from Fig. 3a that the wave height increase in the EEP observed in Fig. 1 is caused by the larger influx of swell from the Southern Ocean.

5. Changes to the Stokes depth and turbulent Langmuir number

The surface Stokes drift and Stokes transport summarize in a compact way changes to the Stokes drift climate, even if they cannot account for veering with depth due to multidirectional wave systems consisting of, for example, swell and local wind sea (Webb and Fox-Kemper 2011, 2015). An important question is how the Stokes drift shear will change, as it is related to the Stokes production in Eq. (4). Since, for a monochromatic Stokes profile,

$$\frac{\partial v_s}{\partial z} = \frac{v_{s0}}{\delta_s} e^{z/\delta_s}, \quad (11)$$

we see that the Stokes depth [Eq. (5)] is approximately inversely proportional to the layer-averaged Stokes shear. It defines the e -folding depth of the Stokes drift and thereby the penetration depth of the Coriolis–Stokes force (Polton et al. 2005). Consequently, when it changes, it directly affects the momentum balance and the advection of tracers. Figure 4 shows the average Stokes depth for the historical period (Fig. 4a) and the relative change for the future RCP8.5 scenario (Fig. 4b). It is interesting to note that the Stokes depth is an order of magnitude larger in the swell-dominated equatorial

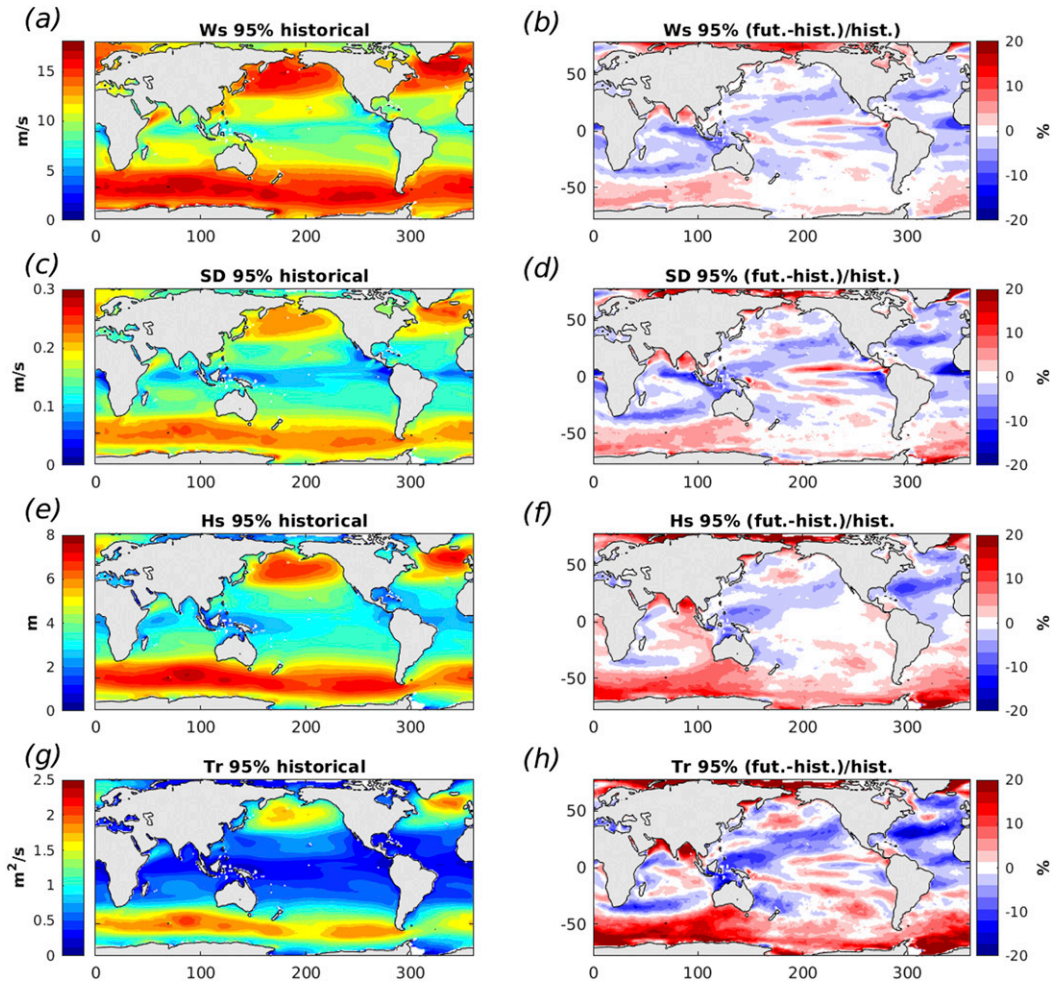


FIG. 2. (a) Annual 95th-percentile 10-m wind speed U_{10} , (c) Stokes drift speed v_{s0} , (e) significant wave height H_s , (g) and Stokes transport V_s from the historical run and (b),(d),(f),(h) the normalized difference (%) between the future RCP8.5 run and the historical run.

regions of the Pacific and Atlantic Oceans than in the wind-sea-dominated Caribbean. This highlights how swell and wind-sea-dominated regions may have similar Stokes transport but widely different Stokes depth climate. The future Stokes depth (Fig. 4b) exhibits a 15% deepening in the Southern Ocean and a shallowing of about 15% in the North Atlantic. These changes are largely driven by changes in swell patterns (cf. Fig. 1h and Fig. 3d).

The average La_t from the historical run is shown in Fig. 4c. An average value of 0.3 is often assumed (McWilliams et al. 1997; Belcher et al. 2012) for the extratropics. This is close to the levels found in the Southern Ocean and the North Atlantic and North Pacific (Fig. 4c). The spatial patterns of La_t are quite similar but of opposite sign to those of δ_s . We see a 5%–10% decrease in La_t in the Southern Ocean and an increase of about 5% in the central North Atlantic (Fig. 4).

Several KPP enhancement factors F_{LT} have been proposed, all based on inverse powers of La_t . To further investigate the expected impact on the turbulent diffusion in the mixed layer of an ocean model, we calculated the long-term average of the enhancement factor [Eq. (8)] proposed by McWilliams and Sullivan (2000) for the historical and the RCP8.5 runs (Fig. 5). The results indicate an enhancement of about 5% for the Southern Ocean and a decrease of 5%–10% in the central North Pacific and a smaller reduction in the North Atlantic.

6. Conclusions

The Stokes drift profile is, to first approximation, a function of the surface Stokes drift and the Stokes transport (Breivik et al. 2014). We have investigated one scenario (RCP8.5) for the future wave climate generated

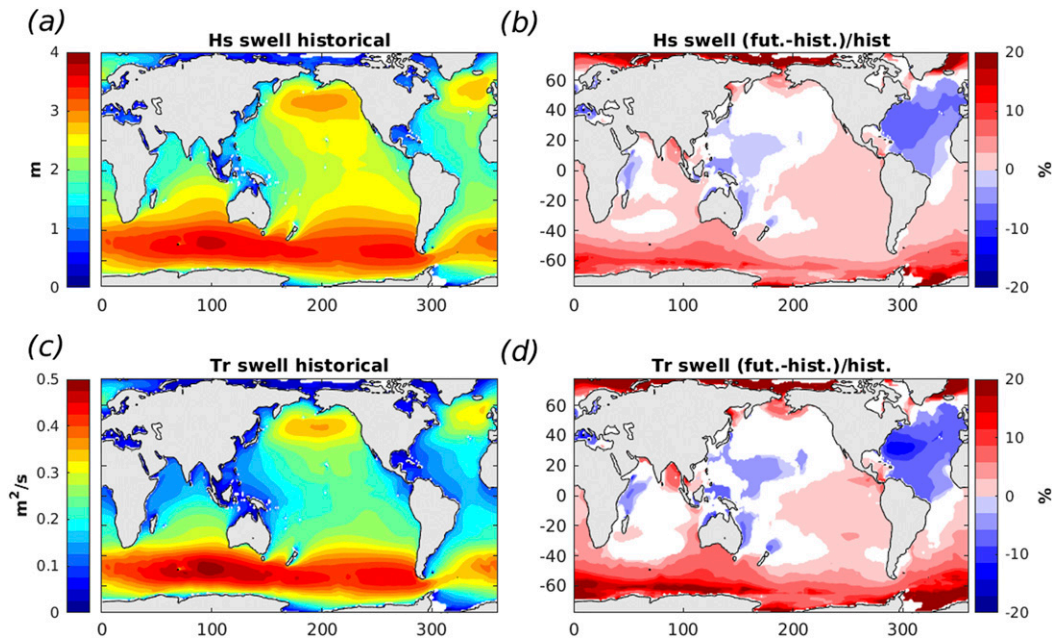


FIG. 3. (a) Average swell wave height and (c) swell Stokes transport from the historical run (1976–2005) and (b),(d) the normalized difference (%) between the future RCP8.5 run (2071–2100) and the historical run. Colored areas have significant differences (significance level: 0.01).

by the EC-EARTH climate model and found that the Southern Ocean can expect an increase in both v_{s0} and V_s of about 15% and 20%, respectively. This increase is stronger than the projected changes to the wind field

(see Fig. 1). Likewise, the decrease in the Northern Hemisphere is stronger than the wind speed decrease. In the case of Stokes drift, we can expect to see increased westerly drift in the Southern Ocean and a weakening in

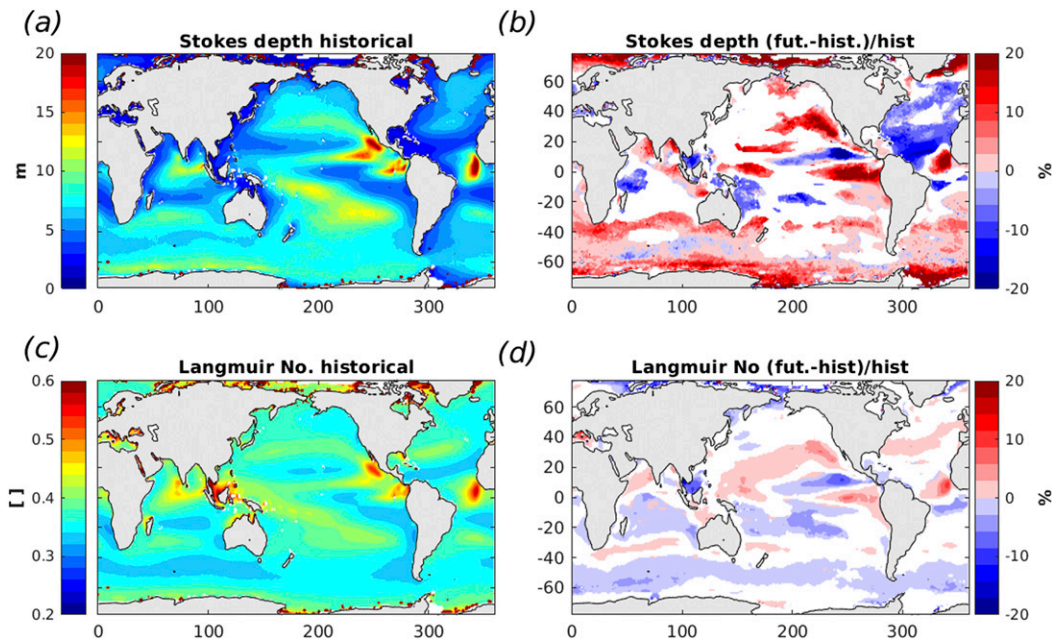


FIG. 4. (a) Average Stokes depth for the historical period. (b) Relative change to Stokes depth under RCP8.5. (c) Average turbulent Langmuir number for historical period. (d) Relative change to the turbulent Langmuir number under RCP8.5. In (b) and (d), only the regions statistically different with a significance level of 0.01 are colored.

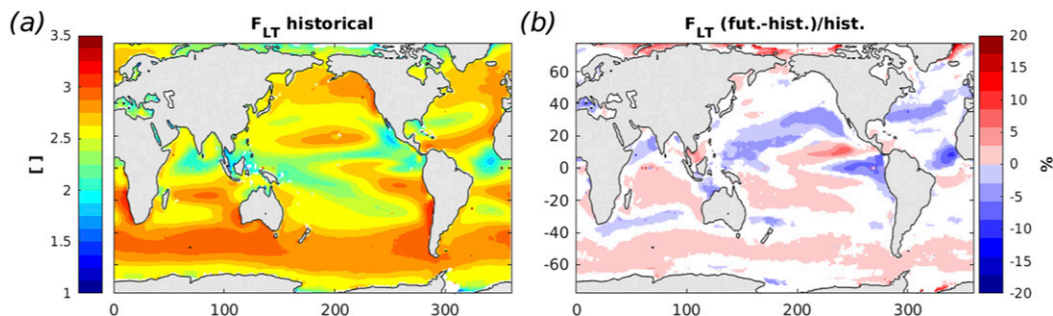


FIG. 5. (a) Average of the Langmuir-enhancement factor F_{LT} [Eq. (8)] proposed by McWilliams and Sullivan (2000) for the historical period (1976–2005). (b) Relative change (%) to F_{LT} under RCP8.5 for the future period (2071–2100) vs the historical period. Only the regions statistically different with a significance level of 0.01 are colored in (b).

the North Atlantic and in parts of the eastern North Pacific. Whether these changes will affect the mixed layer of the ocean depends to some extent on how the swell patterns (see Fig. 3b) change since the total Stokes drift profile is determined by the full wave spectrum, Eq. (1). Recent studies (Van Roekel et al. 2012; McWilliams et al. 2014) point out that the presence of crossing seas (e.g., swell and wind sea propagating in different directions) will affect the depth and strength of Langmuir-induced mixing. If these patterns are found to change significantly, for example, in areas such as the EEP, where we see an increase in significant wave height due to more swell toward the end of this century (see Fig. 1f), we must expect changes to the mixing and the mixed layer depth as well. It is, however, clear that the relation between La_t and the mixing in the upper ocean must be further investigated. The parameterization of the Langmuir-enhancement factor, Eq. (8), originally presented by McWilliams and Sullivan (2000), has been found to be too vigorous (Fan and Griffies 2014; Li et al. 2016; Ali et al. 2018, manuscript submitted to *Ocean Modell.*). Alternative enhancement factors based on the work by, among others, Smyth et al. (2002), Li et al. (2005), Harcourt and D’Asaro (2008), Takaya et al. (2010), and Van Roekel et al. (2012) yield a weaker enhancement by the Langmuir turbulence on the KPP scheme, as shown by Li et al. (2016), Ali et al. (2018, manuscript submitted to *Ocean Modell.*), and Malila (2017). Also important is the mixed layer depth. For example, in wintertime conditions with a deep mixed layer, the additional mixing induced by Langmuir turbulence is unlikely to make much difference (Ali et al. 2018, manuscript submitted to *Ocean Modell.*). This means that although the mixing can be expected to decrease in the northern extratropics and to increase in the Southern Ocean, as seen in Fig. 5b, the actual magnitude of these changes must be investigated by integrating fully coupled models with an active wave model component (Fan and

Griffies 2014; Breivik et al. 2015; Li et al. 2016) under different emission scenarios. However, the differences found for the enhancement parameterization, Eq. (8), are large enough that we can expect to see increased mixing in the Southern Ocean and reduced mixing in the northern extratropics toward the end of the twenty-first century under the RCP8.5 scenario. Similarly, the projected changes of $\pm 10\%$ to the Stokes depth suggest that the changing wave climate may also affect the circulation directly through changes to the near-surface Coriolis–Stokes forcing.

Acknowledgments. This study was carried out in the framework of the Coordinated Ocean Wave Climate Project (COWCLIP) set up by The Joint WMO-IOC Technical Commission for Oceanography and Marine Meteorology (JCOMM). ØB, JRB, and JS gratefully acknowledge support from the Copernicus Marine Environmental Monitoring Service (CMEMS) and Mercator Ocean through the WaveFlow Service Evolution project. The wave climate integrations are archived by MET Norway and HZG (Experiment ID GR4). The hindcast integration is archived in ECMWF’s MARS archive (Experiment ID gowi). AB acknowledges support from the Initiative and Networking Fund of the Helmholtz Association through the project “Advanced Earth System Modelling Capacity (ESM)”, and JS acknowledges support from the European Union H2020 Programme under grant agreement no. H2020-EO-2016-730030-CEASELES.

APPENDIX A

Comparison of the Historical Wave Climate Integration and a Wave Hindcast

There are notable differences between WAM used for the historical run and the EC-WAM hindcast. These differences are significant, and the purpose of the

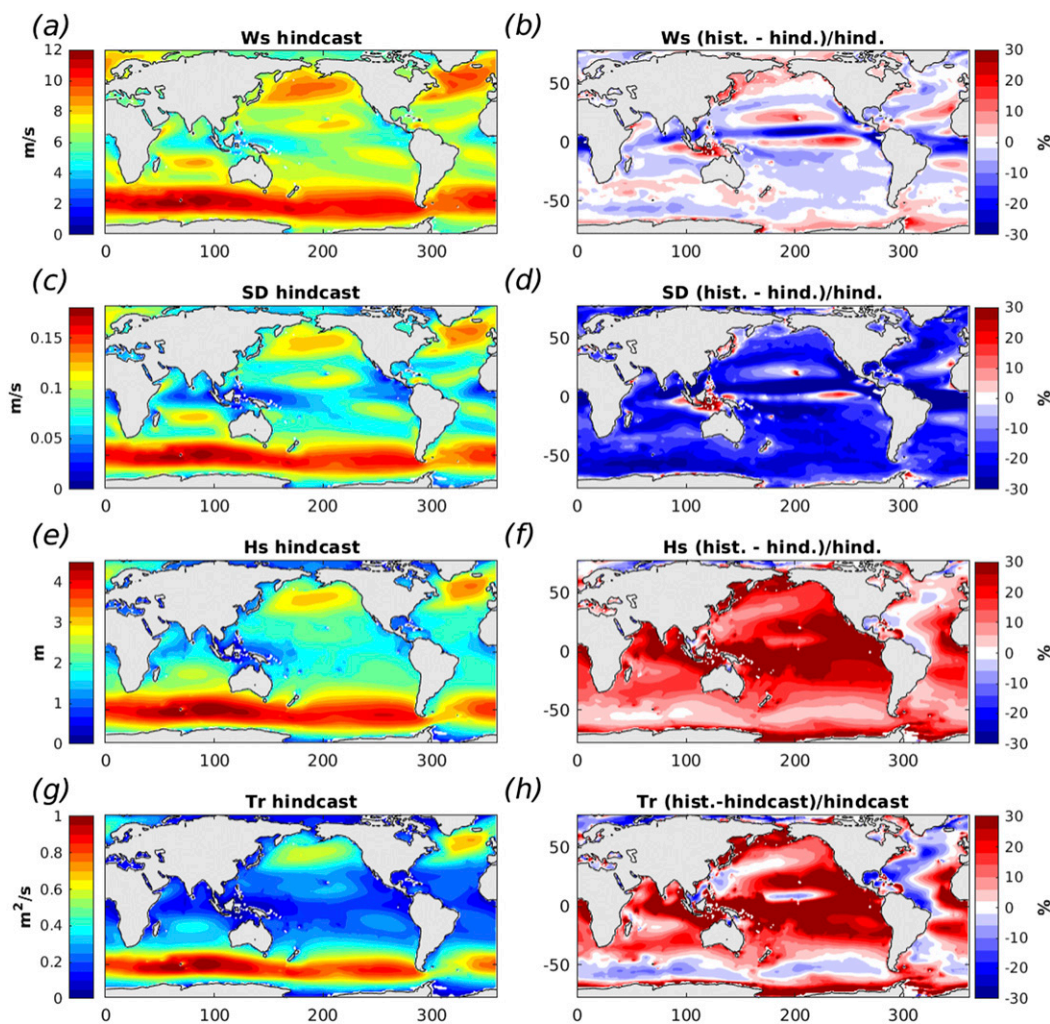


FIG. A1. (a) Annual-average 10-m wind speed U_{10} , (c) Stokes drift speed v_{s0} , (e) significant wave height H_s , and (g) Stokes transport V_s from the hindcast run and (b), (d), (f), (h) the relative difference (%) between the historical experiment and the hindcast run.

comparison is not to look for details of the wave field but rather to assess whether the climate of the historical run broadly corresponds to what can be considered a state-of-the-art global hindcast of the present wave climate and to ascertain that we understand the differences. Importantly, EC-WAM has a subgrid scheme for accounting for unresolved topographic features (most importantly islands). The model runs cover slightly different periods (1999–2016 and 1975–2005), but the historical climate run is not expected to capture year-to-year differences in the past climate record, and we deem these periods to be sufficiently overlapping to allow a meaningful comparison. Moreover, as mentioned above, the version of EC-WAM used for this hindcast contains recent modifications made to incorporate the latest wave physics of [Ardhuin et al. \(2010\)](#), in particular, attenuation of the long swell that propagates into the

tropics and a retuned wind input term with the wave sheltering effect directly accounted for. The hindcast was interpolated using bilinear interpolation to the coarser resolution of the climate run and daily averages were formed for comparison.

The average of the ERA-Interim wind field used to force the wave hindcast is shown in [Fig. A1a](#). [Fig. A1b](#) displays the normalized difference between the EC-EARTH 30-yr average wind field and the hindcast average. The trade wind regions show significant differences in wind speed in relative terms (on the order of 20%), but the winds are generally weak in those regions. The differences in the windier extratropics are on the order of $\pm 10\%$. There are also differences that can be attributed to resolution, such as in the Indonesian archipelago. However, they are not huge, and it is clear that the historical EC-EARTH run agrees reasonably

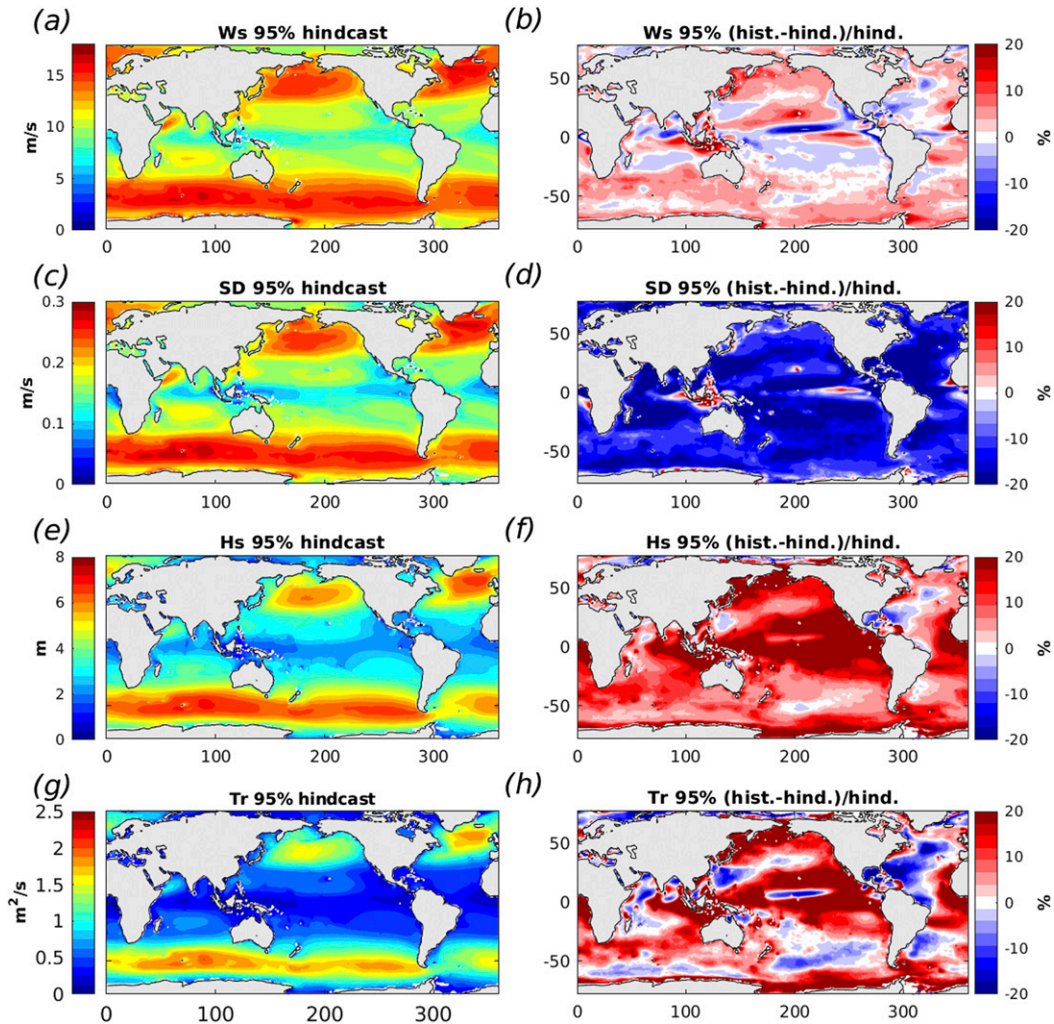


FIG. B1. (a) Annual 95th-percentile 10-m wind speed U_{10} , (c) Stokes drift speed v_{s0} , (e) significant wave height H_s , and (g) Stokes transport V_s from the hindcast run and (b), (d), (f), (h) the relative difference (%) between the historical experiment and the hindcast run.

well with average ERA-Interim surface wind patterns. The historical EC-EARTH wind fields and the historical wave model integration considered here were evaluated against buoys and reanalysis wind by [Semedo et al. \(2018\)](#) and found to be in good agreement. ERA-Interim yields realistic average wind fields, although the trends are known to be unreliable ([Aarnes et al. 2015](#)) because of changes to the observation network.

[Figures A1c and A1d](#) show the surface Stokes drift of the hindcast and the normalized difference of the historical climate run relative to the hindcast, respectively. The surface Stokes drift of the hindcast is larger than that from the historical run almost everywhere. EC-WAM covers a larger range of frequencies (higher and lower frequencies; see [Table 1](#)). This partly explains the differences, as v_{s0} is sensitive to the tail of the spectrum because of its f^3 weighting [see Eq. (1)]. Note that both

models do add a diagnostic high-frequency tail ([ECMWF 2016](#); [Breivik et al. 2014](#)), but as EC-WAM has a much higher frequency range, there can be substantial differences in the amount of energy on the highest prognostic frequency band. As [Breivik et al. \(2014\)](#) reports, the contribution to the surface Stokes drift from the high-frequency (HF) tail may be as high as 30%. However, HF contribution decays rapidly with depth, and consequently, the Stokes transport is almost unaffected [about 3% on average according to [Breivik et al. \(2014\)](#)]. Certain areas stand out, such as the Galapagos Islands and Hawaii, where the historical run has up to 30% higher v_{s0} . These discrepancies stem in part from differences in wind speed, but are exacerbated by the fact that the climate run is unable to resolve the islands where the subgrid scheme of the hindcast effectively reduces the wave energy admitted between unresolved islands.

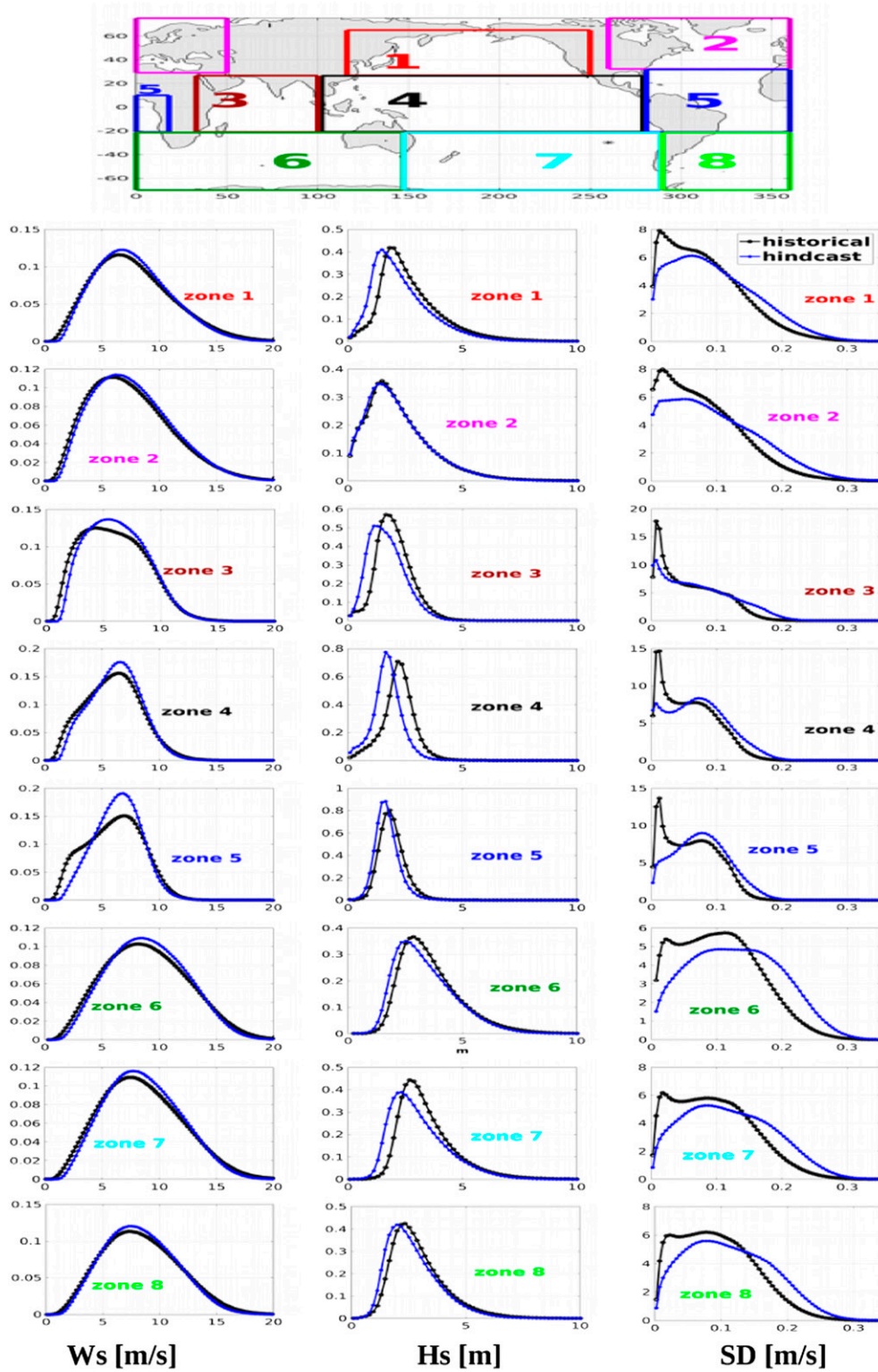


FIG. B2. PDF of daily means of (left) U_{10} , (center) H_s , and (right) v_{50} for different regions. The hindcast run is plotted in blue, and the historical climate run is plotted in black.

The significant wave height (Figs. A1e,f) and Stokes transport (Figs. A1g,h) are more dominated by swell than the surface Stokes drift (Figs. A1c,d). We see that H_s is mostly higher in the historical climate run, on average by about 10%. This has to do with the stronger swell dissipation in EC-WAM (with the ST4 physics employed in this hindcast). This becomes particularly pronounced in the eastern equatorial Pacific where swell propagates from both hemispheres. This is evident in Fig. A1f where we see that the average difference in the eastern Pacific exceeds 25%. The subtropical and tropical latitude range from 40°S to 40°N is dominated by swell, and it is clear that this also affects the Stokes transport (see Figs. A1g, h), which is also larger in the historical run than in the hindcast. These differences are attributable to the different model resolution and the differing physics as well as the model periods, and there is nothing in the difference patterns that suggests that the wave climate model setup should perform better or worse in a future climate.

APPENDIX B

Probability Density Functions and Upper-Percentile Maps

Figure B1 (left panels) present maps of annual 95th-percentile levels for the hindcast (cf. with annual-mean quantities in Fig. A1). The differences (right panels) between the historical run and the hindcast at the 95th-percentile level are found to be quite similar to those between the mean quantities, but the historical run exceeds the hindcast wind speed in a much larger area (see Fig. B1).

Figure B2 shows the probability density function (PDF) from daily means of the wind speed, H_s , and v_{s0} from the historical run (black lines) and the hindcast run (blue lines) for various regions of the world's oceans (see top panel for an overview of the regions). The wind speed PDFs differ mostly in the tropical regions, as suggested by Fig. A1b. The mean H_s from the historical run is almost always higher than the mean from the hindcast that is also in accordance with Fig. A1f. Although the mean v_{s0} of the hindcast is almost always higher than the historical run, also in accordance with Fig. A1d, the shape of the v_{s0} PDF is markedly different from those of H_s and wind speed, and the difference between the hindcast and the historical run is considerable. The almost bimodal shape of the PDF is due to swell, which, in the absence of wind sea, will yield a weak surface Stokes drift. It is clear that the hindcast has a stronger swell dissipation since the occurrence of swell is smaller than the one in the historical run. The other notable difference is in the tail of the PDF where differences are mostly attributable to the higher-frequency cutoff of the hindcast run (see Table 1).

REFERENCES

- Aarnes, O. J., S. Abdalla, J.-R. Bidlot, and Ø. Breivik, 2015: Marine wind and wave height trends at different ERA-Interim forecast ranges. *J. Climate*, **28**, 819–837, <https://doi.org/10.1175/JCLI-D-14-00470.1>.
- , and Coauthors, 2017: Projected changes in significant wave height toward the end of the 21st century: Northeast Atlantic. *J. Geophys. Res. Oceans*, **122**, 3394–3403, <https://doi.org/10.1002/2016JC012521>.
- Alari, V., J. Staneva, Ø. Breivik, J.-R. Bidlot, K. Mogensen, and P. Janssen, 2016: Surface wave effects on water temperature in the Baltic Sea: Simulations with the coupled NEMO-WAM model. *Ocean Dyn.*, **66**, 917–930, <https://doi.org/10.1007/s10236-016-0963-x>.
- Arduhin, F., L. Marié, N. Rasclé, P. Forget, and A. Roland, 2009: Observation and estimation of Lagrangian, Stokes, and Eulerian Currents induced by wind and waves at the sea surface. *J. Phys. Oceanogr.*, **39**, 2820–2838, <https://doi.org/10.1175/2009JPO4169.1>.
- , and Coauthors, 2010: Semiempirical dissipation source functions for ocean waves. Part I: Definition, calibration, and validation. *J. Phys. Oceanogr.*, **40**, 1917–1941, <https://doi.org/10.1175/2010JPO4324.1>.
- Belcher, S. E., and Coauthors, 2012: A global perspective on Langmuir turbulence in the ocean surface boundary layer. *Geophys. Res. Lett.*, **39**, L18605, <https://doi.org/10.1029/2012GL052932>.
- Bidlot, J., P. Janssen, and S. Abdalla, 2007: A revised formulation of ocean wave dissipation and its model impact. ECMWF Tech. Memo. 509, 27 pp.
- Bitner-Gregersen, E., and Coauthors, 2018: Climate change and safe design of ship structures. *Ocean Eng.*, **149**, 226–237, <https://doi.org/10.1016/j.oceaneng.2017.12.023>.
- Breivik, Ø., A. A. Allen, C. Maisondieu, and M. Olagnon, 2013: Advances in search and rescue at sea. *Ocean Dyn.*, **63**, 83–88, <https://doi.org/10.1007/s10236-012-0581-1>.
- , P. A. E. M. Janssen, and J.-R. Bidlot, 2014: Approximate Stokes drift profiles in deep water. *J. Phys. Oceanogr.*, **44**, 2433–2445, <https://doi.org/10.1175/JPO-D-14-0020.1>.
- , K. Mogensen, J.-R. Bidlot, M. A. Balmaseda, and P. A. E. M. Janssen, 2015: Surface wave effects in the Nemo ocean model: Forced and coupled experiments. *J. Geophys. Res. Oceans*, **120**, 2973–2992, <https://doi.org/10.1002/2014JC010565>.
- , J.-R. Bidlot, and P. A. E. M. Janssen, 2016: A Stokes drift approximation based on the Phillips spectrum. *Ocean Modell.*, **100**, 49–56, <https://doi.org/10.1016/j.ocemod.2016.01.005>.
- Carrasco, A., A. Semedo, P. E. Isachsen, K. H. Christensen, and Ø. Sætra, 2014: Global surface wave drift climate from ERA-40: The contributions from wind-sea and swell. *Ocean Dyn.*, **64**, 1815–1829, <https://doi.org/10.1007/s10236-014-0783-9>.
- Cavaleri, L., B. Fox-Kemper, and M. Hemer, 2012: Wind waves in coupled climate systems. *Bull. Amer. Meteor. Soc.*, **93**, 1651–1661, <https://doi.org/10.1175/BAMS-D-11-00170.1>.
- , and Coauthors, 2018: Wave modelling in coastal and inner seas. *Prog. Oceanogr.*, **167**, 164–233, <https://doi.org/10.1016/j.pocean.2018.03.010>.
- Dagestad, K.-F., J. Röhrs, Ø. Breivik, and B. Ådlandsvik, 2018: OpenDrift v1.0: A generic framework for trajectory modeling. *Geosci. Model Dev.*, **11**, 1405–1420, <https://doi.org/10.5194/gmd-11-1405-2018>.

- D'Asaro, E. A., J. Thomson, A. Y. Shcherbina, R. R. Harcourt, M. F. Cronin, M. A. Hemer, and B. Fox-Kemper, 2014: Quantifying upper ocean turbulence driven by surface waves. *Geophys. Res. Lett.*, **41**, 102–107, <https://doi.org/10.1002/2013GL058193>.
- Dee, D. P., and Coauthors, 2011: The ERA-Interim reanalysis: Configuration and performance of the data assimilation system. *Quart. J. Roy. Meteor. Soc.*, **137**, 553–597, <https://doi.org/10.1002/qj.828>.
- ECMWF, 2016: IFS Documentation—CY43r1, Part VII: ECMWF wave model. ECMWF Doc. 99 pp., <https://www.ecmwf.int/sites/default/files/elibrary/2016/17120-part-vii-ecmwf-wave-model.pdf>.
- Fan, Y., and S. M. Griffies, 2014: Impacts of parameterized Langmuir turbulence and nonbreaking wave mixing in global climate simulations. *J. Climate*, **27**, 4752–4775, <https://doi.org/10.1175/JCLI-D-13-00583.1>.
- Flór, J. B., E. J. Hopfinger, and E. Guyez, 2010: Contribution of coherent vortices such as Langmuir cells to wind-driven surface layer mixing. *J. Geophys. Res.*, **115**, C10031, <https://doi.org/10.1029/2009JC005900>.
- Gibbons, J. D., and S. Chakraborti, 2011: Nonparametric statistical inference. *International Encyclopedia of Statistical Science*, M. Lovric, Ed., Springer, 977–979, https://doi.org/10.1007/978-3-642-04898-2_420.
- Hanley, K. E., S. E. Belcher, and P. P. Sullivan, 2010: A global climatology of wind–wave interaction. *J. Phys. Oceanogr.*, **40**, 1263–1282, <https://doi.org/10.1175/2010JPO4377.1>.
- Harcourt, R. R., and E. A. D'Asaro, 2008: Large-eddy simulation of Langmuir turbulence in pure wind seas. *J. Phys. Oceanogr.*, **38**, 1542–1562, <https://doi.org/10.1175/2007JPO3842.1>.
- Hasselmann, S., and Coauthors, 1988: The WAM Model—A third generation ocean wave prediction model. *J. Phys. Oceanogr.*, **18**, 1775–1810, [https://doi.org/10.1175/1520-0485\(1988\)018<1775:TWMTGO>2.0.CO;2](https://doi.org/10.1175/1520-0485(1988)018<1775:TWMTGO>2.0.CO;2).
- Hazeleger, W., and Coauthors, 2010: EC-Earth: A seamless Earth-system prediction approach in action. *Bull. Amer. Meteor. Soc.*, **91**, 1357–1363, <https://doi.org/10.1175/2010BAMS2877.1>.
- , and Coauthors, 2012: EC-Earth V2.2: Description and validation of a new seamless Earth system prediction model. *Climate Dyn.*, **39**, 2611–2629, <https://doi.org/10.1007/s00382-011-1228-5>.
- Hemer, M. A., Y. Fan, N. Mori, A. Semedo, and X. L. Wang, 2013: Projected changes in wave climate from a multi-model ensemble. *Nat. Climate Change*, **3**, 471–476, <https://doi.org/10.1038/nclimate1791>.
- Hersbach, H., and P. A. E. M. Janssen, 1999: Improvement of the short-fetch behavior in the Wave Ocean Model (WAM). *J. Atmos. Oceanic Technol.*, **16**, 884–892, [https://doi.org/10.1175/1520-0426\(1999\)016<0884:IOTSFB>2.0.CO;2](https://doi.org/10.1175/1520-0426(1999)016<0884:IOTSFB>2.0.CO;2).
- Holthuijsen, L., 2007: *Waves in Oceanic and Coastal Waters*. Cambridge University Press, 387 pp.
- Janssen, P. A. E. M., 2012: Ocean wave effects on the daily cycle in SST. *J. Geophys. Res.*, **117**, C00J32, <https://doi.org/10.1029/2012JC007943>.
- Jones, C. E., and Coauthors, 2016: Measurement and modeling of oil slick transport. *J. Geophys. Res. Oceans*, **121**, 7759–7775, <https://doi.org/10.1002/2016JC012113>.
- Kantha, L. H., and C. A. Clayson, 2000: *Small Scale Processes in Geophysical Fluid Flows*. International Geophysics, Vol. 67, Academic Press, 750 pp.
- Kenyon, K. E., 1969: Stokes drift for random gravity waves. *J. Geophys. Res.*, **74**, 6991–6994, <https://doi.org/10.1029/JC074i028p06991>.
- Komen, J., L. Cavaleri, M. Donelan, K. Hasselmann, and P. A. E. M. Janssen, 1994: *Dynamics and Modelling of Ocean Waves*. Cambridge University Press, 560 pp., <https://doi.org/10.1017/S0022112096220166>.
- Kukulka, T., and R. R. Harcourt, 2017: Influence of Stokes drift decay scale on Langmuir turbulence. *J. Phys. Oceanogr.*, **47**, 1637–1656, <https://doi.org/10.1175/JPO-D-16-0244.1>.
- Large, W. G., J. C. McWilliams, and S. C. Doney, 1994: Oceanic vertical mixing: A review and a model with a nonlocal boundary layer parameterization. *Rev. Geophys.*, **32**, 363–403, <https://doi.org/10.1029/94RG01872>.
- Li, M., and C. Garrett, 1997: Mixed layer deepening due to Langmuir circulation. *J. Phys. Oceanogr.*, **27**, 121–132, [https://doi.org/10.1175/1520-0485\(1997\)027<0121:MLDDTL>2.0.CO;2](https://doi.org/10.1175/1520-0485(1997)027<0121:MLDDTL>2.0.CO;2).
- , —, and E. Skillingstad, 2005: A regime diagram for classifying turbulent large eddies in the upper ocean. *Deep-Sea Res. I*, **52**, 259–278, <https://doi.org/10.1016/j.dsr.2004.09.004>.
- Li, Q., and B. Fox-Kemper, 2017: Assessing the effects of Langmuir turbulence on the entrainment buoyancy flux in the ocean surface boundary layer. *J. Phys. Oceanogr.*, **47**, 2863–2886, <https://doi.org/10.1175/JPO-D-17-0085.1>.
- , A. Webb, B. Fox-Kemper, A. Craig, G. Danabasoglu, W. G. Large, and M. Vertenstein, 2016: Langmuir mixing effects on global climate: WAVEWATCH III in CESM. *Ocean Modell.*, **103**, 145–160, <https://doi.org/10.1016/j.ocemod.2015.07.020>.
- , B. Fox-Kemper, Ø. Breivik, and A. Webb, 2017: Statistical models of global Langmuir mixing. *Ocean Modell.*, **113**, 95–114, <https://doi.org/10.1016/j.ocemod.2017.03.016>.
- Malila, M. P., 2017: Langmuir turbulence in the HYCOM ocean model. M.S. thesis, Geophysical Institute, University of Bergen, 131 pp.
- McWilliams, J. C., and P. P. Sullivan, 2000: Vertical mixing by Langmuir circulations. *Spill Sci. Technol. Bull.*, **6**, 225–237, [https://doi.org/10.1016/S1353-2561\(01\)00041-X](https://doi.org/10.1016/S1353-2561(01)00041-X).
- , —, and C.-H. Moeng, 1997: Langmuir turbulence in the ocean. *J. Fluid Mech.*, **334**, 1–30, <https://doi.org/10.1017/S0022112096004375>.
- , E. Huckle, J. Liang, and P. P. Sullivan, 2014: Langmuir turbulence in swell. *J. Phys. Oceanogr.*, **44**, 870–890, <https://doi.org/10.1175/JPO-D-13-0122.1>.
- Noh, Y., H. Ok, E. Lee, T. Toyoda, and N. Hirose, 2016: Parameterization of Langmuir circulation in the ocean mixed layer model using LES and its application to the OGCM. *J. Phys. Oceanogr.*, **46**, 57–78, <https://doi.org/10.1175/JPO-D-14-0137.1>.
- Pierson, W. J., Jr., and L. Moskowitz, 1964: A proposed spectral form for fully developed wind seas based on the similarity theory of S. A. Kitaigorodskii. *J. Geophys. Res.*, **69**, 5181–5190, <https://doi.org/10.1029/JZ069i024p05181>.
- Polton, J. A., D. M. Lewis, and S. E. Belcher, 2005: The role of wave-induced Coriolis–Stokes forcing on the wind-driven mixed layer. *J. Phys. Oceanogr.*, **35**, 444–457, <https://doi.org/10.1175/JPO2701.1>.
- Röhrs, J., K. H. Christensen, L. R. Hole, G. Broström, M. Drivdal, and S. Sundby, 2012: Observation-based evaluation of surface wave effects on currents and trajectory forecasts. *Ocean Dyn.*, **62**, 1519–1533, <https://doi.org/10.1007/s10236-012-0576-y>.
- , —, F. Vikebø, S. Sundby, Ø. Saetra, and G. Broström, 2014: Wave-induced transport and vertical mixing of pelagic eggs and larvae. *Limnol. Oceanogr.*, **59**, 1213–1227, <https://doi.org/10.4319/lo.2014.59.4.1213>.
- , A. K. Sperrevik, K. H. Christensen, G. Broström, and Ø. Breivik, 2015: Comparison of HF radar measurements with Eulerian and Lagrangian surface currents. *Ocean Dyn.*, **65**, 679–690, <https://doi.org/10.1007/s10236-015-0828-8>.

- Semedo, A., and Coauthors, 2018: CMIP5-derived single-forcing, single-model, and single-scenario wind-wave climate ensemble: Configuration and performance evaluation. *J. Mar. Sci. Eng.*, **6**, 90, <https://doi.org/10.3390/jmse6030090>.
- Shimura, T., N. Mori, and M. A. Hemer, 2016: Variability and future decreases in winter wave heights in the western North Pacific. *Geophys. Res. Lett.*, **43**, 2716–2722, <https://doi.org/10.1002/2016GL067924>.
- Smyth, W. D., E. D. Skillingstad, G. B. Crawford, and H. Wijesekera, 2002: Nonlocal fluxes and Stokes drift effects in the K-profile parameterization. *Ocean Dyn.*, **52**, 104–115, <https://doi.org/10.1007/s10236-002-0012-9>.
- Staneva, J., V. Alari, Ø. Breivik, J.-R. Bidlot, and K. Mogensen, 2017: Effects of wave-induced forcing on a circulation model of the North Sea. *Ocean Dyn.*, **67**, 81–101, <https://doi.org/10.1007/s10236-016-1009-0>.
- Stocker, T., and Coauthors, 2013: Technical summary. *Climate Change 2013: The Physical Science Basis*, T. F. Stocker et al., Eds., Cambridge University Press, 33–115, https://www.ipcc.ch/site/assets/uploads/2018/02/WG1AR5_TS_FINAL.pdf.
- Stokes, G. G., 1847: On the theory of oscillatory waves. *Trans. Cambridge Philos. Soc.*, **8**, 441–455.
- Strand, K., F. Vikebø, S. Sundby, A. Sperrevik, and Ø. Breivik, 2018: Sub-surface maxima in buoyant fish eggs indicate vertical velocity shear and spatially limited spawning grounds. *Limnol. Oceanogr.*, <https://doi.org/10.1002/lno.11109>, in press.
- Stull, R. B., 1988: *An Introduction to Boundary Layer Meteorology*. Kluwer, 666 pp.
- Sutherland, G., K. H. Christensen, and B. Ward, 2014: Evaluating Langmuir turbulence parameterizations in the ocean surface boundary layer. *J. Geophys. Res. Oceans*, **119**, 1899–1910, <https://doi.org/10.1002/2013JC009537>.
- Suzuki, N., and B. Fox-Kemper, 2016: Understanding Stokes forces in the wave-averaged equations. *J. Geophys. Res. Oceans*, **121**, 3579–3596, <https://doi.org/10.1002/2015JC011566>.
- Takaya, Y., J.-R. Bidlot, A. C. M. Beljaars, and P. A. E. M. Janssen, 2010: Refinements to a prognostic scheme of skin sea surface temperature. *J. Geophys. Res.*, **115**, C06009, <https://doi.org/10.1029/2009JC005985>.
- van den Bremer, T., and Ø. Breivik, 2017: Stokes drift. *Philos. Trans. Roy. Soc. London*, **376A**, 20170104, <https://doi.org/10.1098/rsta.2017.0104>.
- Van Roekel, L. P., B. Fox-Kemper, P. P. Sullivan, P. E. Hamlington, and S. R. Haney, 2012: The form and orientation of Langmuir cells for misaligned winds and waves. *J. Geophys. Res.*, **117**, C05001, <https://doi.org/10.1029/2011JC007516>.
- Wang, X. L., Y. Feng, and V. R. Swail, 2014: Changes in global ocean wave heights as projected using multimodel CMIP5 simulations. *Geophys. Res. Lett.*, **41**, 1026–1034, <https://doi.org/10.1002/2013GL058650>.
- Webb, A., and B. Fox-Kemper, 2011: Wave spectral moments and Stokes drift estimation. *Ocean Modell.*, **40**, 273–288, <https://doi.org/10.1016/j.ocemod.2011.08.007>.
- , and —, 2015: Impacts of wave spreading and multidirectional waves on estimating Stokes drift. *Ocean Modell.*, **96**, 49–64, <https://doi.org/10.1016/j.ocemod.2014.12.007>.